

Unravelling unsaturated edge S in amorphous NiS_x for boosting photocatalytic H₂ evolution of metastable phase CdS confined inside hydrophilic beads

Yizhong Zhang ^{a,g}, Wei Zhou ^c, Yuan Tang ^a, Yuchen Guo ^a, Zikang Geng ^b, Lequan Liu ^e, Xin Tan ^{a,d}, Huaiyuan Wang ^b, Tao Yu ^{b,e,*}, Jinhua Ye ^{e,f}

^a School of Environmental Science and Engineering, Tianjin University, No. 135 Yaguan Road, Jinnan District, Tianjin 300350, People's Republic of China

^b School of Chemical Engineering and Technology, Tianjin University, No. 135 Yaguan Road, Jinnan District, Tianjin 300350, People's Republic of China

^c School of Science, Tianjin University, No. 135 Yaguan Road, Jinnan District, Tianjin 300350, People's Republic of China

^d School of Science, Tibet University, No. 36 Jiangsu Road, Lhasa 850000, People's Republic of China

^e TJU-NIMS International Collaboration Laboratory, Tianjin University, No. 92 Weijin Road, Nankai District, Tianjin 300072, People's Republic of China

^f International Center for Materials Nanoarchitectonics (WPI-MANA), National Institute for Materials Science (NIMS), 1-1 Namiki, Tsukuba, Ibaraki 305-0044, Japan

^g The Institute of Seawater Desalination and Multipurpose Utilization, Ministry of Natural Resources (MNR), No. 55 Hanghai Road, Nankai District, Tianjin 300192, People's Republic of China

ARTICLE INFO

Keywords:

Amorphous nickel sulfide
Cadmium sulfide
Chitosan hydrogel beads
Unsaturated S site
Photocatalytic H₂ evolution

ABSTRACT

The unsaturated edge S in the cocatalyst plays an important role in the enrichment of both protons and electrons during the photocatalytic hydrogen evolution process. However, a mild and simple strategy for effectively exposing edge S is still a significant challenge. Herein, amorphous nickel sulfide (NiS_x) as an efficient cocatalyst was decorated on the cubic phase CdS surface, which were confined growth inside hydrophilic chitosan hydrogel beads (CHB@CdS-NiS_x) for efficient and durable photocatalytic H₂ evolution. The optimal CHB@CdS-0.02NiS_x achieved a photocatalytic activity of 11.88 mmol/h/g and displayed ultra-long stability of 60 h. NiS_x could effectively accelerate the electron migration from CdS to NiS_x in composite photocatalyst and provide abundant unsaturated edge active S as H₂-evolution sites. Further density functional theory (DFT) calculation revealed that NiS_x lowered activation energy for H₂O dissociation to boost the local proton concentration, thereby facilitating the activity of H₂ evolution. This study highlights the significance of amorphization strategy for consciously modulating edge sulfur of transition metal sulfide cocatalysts to improve the photocatalytic performance.

1. Introduction

Photocatalytic water splitting to produce hydrogen has long been recognized as an efficient and sustainable solution for building a clean and renewable energy system [1–3]. In order to achieve this goal, it is of great significance to develop a photocatalyst with high chemical stability and activity [4,5]. As a typical visible-light response photocatalyst, CdS has attracted great attention in the field of photocatalytic hydrogen production due to its suitable energy band structure [6,7]. However, a single CdS often cannot achieve high hydrogen production rate, which is caused by its severe photocorrosion and rapid recombination of photo-induced carriers [8,9]. The cocatalyst modification has been proved to be an effective strategy for separation of electron-hole

pairs and providing more proton enrichment and reductions sites [10]. It is undeniable that some noble metals (such as Pt [11], Pd [12], and Au [13]) could be used the efficient cocatalysts for CdS due to their excellent conductivity and near-zero Gibbs free energy of hydrogen adsorption [14]. Unfortunately, the low earth reserves and high cost restrict the future scale-up application of these photocatalyst/cocatalyst systems [15]. Therefore, it is valuable to develop earth-abundance and cost-effective cocatalysts for CdS to boost H₂ evolution reaction.

Transition metal sulfides such as MoS₂ [16,17], NiS [18,19], CuS [20] and WS₂ [21,22] have been used as cocatalysts to improve the photocatalytic H₂ production. Among them, NiS has attracted great interest as alternative cocatalysts for photocatalytic H₂ evolution due to its low cost and good conductivity for photo-generated electrons transport

* Corresponding author at: School of Chemical Engineering and Technology, Tianjin University, No. 135 Yaguan Road, Jinnan District, Tianjin 300350, People's Republic of China.

E-mail address: yutao@tju.edu.cn (T. Yu).

[18,19,23–26]. Previous studies have found that the active sites for efficient hydrogen production in NiS mainly come from the active S sites on the edge of NiS, which could serve as the acceptor centers for both electrons and protons [14]. Therefore, how to effectively expose edge active S sites on the NiS will be the key to improving the performance of hydrogen production. However, the traditional crystalline phase NiS can only expose limited edge active S due to its regular crystal structure and large bulk size, which limits the improvement of hydrogen production performance.

Actually, some strategies have been reported for expanding active S edge of the traditional crystalline phase NiS, including low-dimensional structure construction, morphology control, and S-rich surface construction, to obtain greater photocatalytic hydrogen production activity [27]. Recently, amorphous materials have attracted wide attention in fields of electrocatalysis [28], photocatalysis [29,30], batteries [31], capacitors [32], and adsorption [33] due to its unique superiorities of simple and mild preparation, high specific surface area, more flexible composition adjustment [34–36]. More importantly, benefiting from irregular loose structure, amorphous materials possess abundant coordination unsaturated sites and active sites even can extend from the surface to the bulk of the material [36], which has been confirmed higher photocatalytic H₂ evolution when amorphous cocatalyst was supported on photocatalyst surface. For instance, when amorphous NiS (NiS_x) was used as a cocatalyst of TiO₂ [14] or g-C₃N₄ [37,38], it significantly promoted the separation ability of photogenerated carriers derived from photocatalysts and strengthened the performance of hydrogen production. Unfortunately, to best to our knowledge, systematic study of the photocatalytic hydrogen production of NiS_x-decorated cubic phase CdS system has not been reported. In addition, S²⁻ on the surface of the CdS is easily oxidized by its photo-induced holes in the process of photocatalytic hydrogen production, which triggers photo-corrosion and deteriorates the performance of hydrogen production. Therefore, for NiS_x-decorated CdS systems, the durability of hydrogen production performance needs to be further improved.

Herein, NiS_x-decorated cubic phase CdS system was built inside the hydrophilic chitosan hydrogel beads (CHB@CdS-NiS_x) by two successive adsorption-sulfurization processes under room temperature and investigate its activity of photocatalytic H₂ evolution. X-ray photoelectron spectroscopy (XPS) and electron paramagnetic resonance (EPR) characterization analysis revealed that there were abundant unsaturated edge S sites distributed on the surface of NiS_x, which served as enrichment centers of protons and electrons to enhance the hydrogen production performance. The optimal CHB@CdS-0.02NiS_x achieved a hydrogen production performance of 11.88 mmol/h/g which was approximately 3.2 times that of CHB@CdS and maintained an excellent performance stability after 11 cycles within 60 h. Finally, the more feasible H₂ evolution path (H₂O→H⁺→H₂) on NiS_x was determined by DFT calculation.

2. Experimental section

2.1. Materials and reagents

All reagents, including chitosan [(C₆H₁₁NO₄)_n, molecular weight = 70–80 × 10⁴, deacetylation degree ≥ 90%, Shanghai Lanji Biotechnology], anhydrous acetic acid (CH₃COOH, AR, Shanghai Aladdin), sodium hydroxide (NaOH, AR, Shanghai Aladdin), cadmium acetate [Cd (CH₃COO)₂·2H₂O, AR, Shanghai Aladdin], nickel acetate [Ni (CH₃COO)₂·4H₂O, AR, Tianjin Heowns Biochemical Technology], sodium sulfide (Na₂S·9H₂O, AR, Shanghai Meryer), and sodium sulfite (Na₂SO₃, AR, Shanghai Aladdin) were used as received without further purification.

2.2. Sample preparation

2.2.1. Preparation of CdS confined inside chitosan hydrogel beads (CHB@CdS)

First, chitosan hydrogel beads (CHB) were synthesized following the procedures: 3.0 g of chitosan powder was added to the 100 mL acetic acid solution (0.5 vol%), and then intense agitation to obtain chitosan hydrosol. Under slow magnetic stirring, the hydrosol was added to 500 mL of sodium hydroxide (2 mol/L) by syringe, the white CHB were formed rapidly. After dropping, it continued to solidify for 5 h. Washed with deionized water until neutral pH value and stored it in deionized water for standby; the 10.0 g of CHB were added to the 50 mL, 0.05 mol/L Cd²⁺ solution. After adsorption of 2 h under gentle magnetic stirring, it was separated by filter screen, washed with deionized water for 3 times, then added to 50 mL, 0.4 mol/L of Na₂S solution, sulfurized for 12 h at room temperature, cleaned with deionized water for 5 times, and then stored in deionized water, labeled as CHB@CdS.

2.2.2. In situ growth of amorphous NiS_x on CHB@CdS (CHB@CdS-NiS_x)

10.0 g of the above prepared CHB@CdS was add to 100 mL of Ni²⁺ solution with different concentrations (5, 10, 20 and 40 mmol/L). After adsorption for 1 h, separated it with filter screen, and washed it for 6 times by deionized water to remove residual Ni²⁺ ions, and then transferred to 100 mL, 0.4 mol/L Na₂S solution, sulfurized for 2 h at room temperature. After the reaction was over, filtered by the filter screen, washed with deionized water for 3 times, stored in deionized water, sealed for standby, in which amorphous NiS_x was grown *in situ* on CHB@CdS, these samples were simply described as CHB@CdS-NiS_x.

To obtain the molar ratio of element Ni to Cd in the CHB@CdS-NiS_x, these series of samples were dissolved in nitric acid (2 mol/L), and the concentration of Ni²⁺ and Cd²⁺ in the dissolved solution was determined by an inductively coupled plasma optical emission spectrometer (ICP-OES, iCAP7000 series, Thermo). The experimental measurement found that the molar ratios of Ni to Cd in the CHB@CdS-NiS_x prepared with different Ni²⁺ concentrations of 5, 10, 20, and 40 mmol/L were 0.01, 0.02, 0.05, and 0.12, respectively. For the convenience of discussion, they were abbreviated as CHB@CdS-0.01NiS_x, CHB@CdS-0.02NiS_x, CHB@CdS-0.05NiS_x, and CHB@CdS-0.12NiS_x, respectively. For comparison, the CHB@CdS containing CoS_x, CuS_x, and FeS_x were also prepared in Text S1 in the Supplementary Material.

2.3. Materials characterization

X-ray diffractometer (XRD, Bruker D8-Focus, Germany) was used to determine the phase structure of the synthesized CHB@CdS-NiS_x series samples. A Fourier transform infrared spectrometer (FT-IR, IRAffinity-1S, Japan) was used to obtain the infrared spectra of the synthesized samples. Scanning electron microscope (SEM, S-4800, Japan) and transmission electron microscope (TEM, FEI Tecnai G2 F20, Netherlands) were adopted for observing the microstructure and lattice fringes of the samples. X-ray photoelectron spectroscopy (XPS, Thermo Scientific ESCALAB-250Xi, USA) was utilized for analysis the elemental composition and elemental combining state of the samples. Ultraviolet-visible diffuse reflectance spectra (UV-vis DRS) of the samples were recorded on an ultraviolet-visible spectrophotometer (UV-3600, Shimadzu, Japan), and the measurement range was 220–800 nm. An electron paramagnetic resonance spectrometer (EPR, JES-FA200, Japan) was used to characterize the unsaturated S sites on NiS_x. The photoluminescence (PL) spectra of the samples were gained by a fluorescence spectrometer (Fluorolog-3, USA) with λ_{ex} = 330 nm. Raman spectrometer (XPLORA plus, France) was used to record the Raman spectra of series samples at λ_{ex} = 532 nm. The Kelvin probe force microscope (KPFM) was used in the scanning probe microscope (SPM) system (Bruker Dimension icon, Germany) to measure the surface potential distribution of CHB@CdS-0.02NiS_x under dark and visible light (λ ≥ 420 nm) irradiation conditions. In addition, photoelectrochemical

measurements were also carried out, and detailed methods were presented in the Text S2 in the Supplementary Material.

2.4. Computational details

In this work, all calculations were performed with Vienna *Ab-initio* Simulation Package (VASP) based on the density functional theory (DFT) [39]. The generalized gradient approximation (GGA) with PBE functional was used for the exchange-correlation energy. A plane-wave expansion for the basis set with a cutoff energy of 450 eV was employed. The $3 \times 2 \times 1$ and $7 \times 7 \times 1$ Gamma centered k-point meshes was used for the Brillouin-zone integrations of surface supercell models. All atoms are relaxed until the residual force was less than 0.01 eV/Å. To avoid the periodic interaction along out-plane direction, a vacuum layer of 16 Å was used for the slab model.

The adsorption energy (E_{ads}) of water molecule on the surface of the Slab model can be calculated by the following formula (Eq. 1):

$$E_{\text{ads}} = E_{H_2O+\text{Slab}} - (E_{H_2O} + E_{\text{Slab}}) \quad (1)$$

where, E_{H_2O} , E_{Slab} , and $E_{H_2O+\text{Slab}}$ are the total energies of free water molecule, isolated surface Slab (chitosan, CdS, NiS_x , or NiS), and the Slab that absorbs water molecule ($H_2O+\text{Slab}$ complexes), respectively.

The energies of isolated H_2 and OH molecules were calculated to obtain the binding energies of hydrogen (E_{H}) and hydroxide ions (E_{OH}). The Gibbs free energies of water dissociation and hydrogen adsorption were calculated with total energy (E), zero-point energy (ZPE), environment temperature (T), and entropy (S) via Eq. (2) [40]:

$$\Delta G = \Delta E + \Delta ZPE - T\Delta S \quad (2)$$

2.5. Photocatalytic hydrogen evolution test

2.5 g of the photocatalyst (for CHB@CdS-0.02 NiS_x , through element analysis, the effective contents of CdS and NiS_x were 15.80 mg and 2.62 mg, respectively) was added to a Pyrex glass reaction cell containing 300 mL of sacrificial agent (mixed solution of 0.35 mol/L Na_2S and 0.25 mol/L Na_2SO_3), and the photocatalytic hydrogen evolution reaction system (Shanghai Boyi Scientific Instrument Co. Ltd., China) was performed with vacuum treatment for 30 min before the hydrogen evolution test to remove residual gas. The temperature of the reaction system was controlled at about 10 °C through the circulating cooling water system. The hydrogen evolution reaction was carried out under visible light ($\lambda \geq 420$ nm) irradiation and the hydrogen content was analyzed by an online gas chromatography (GC-2014AT 230V R, Shimadzu Co. Ltd., Japan).

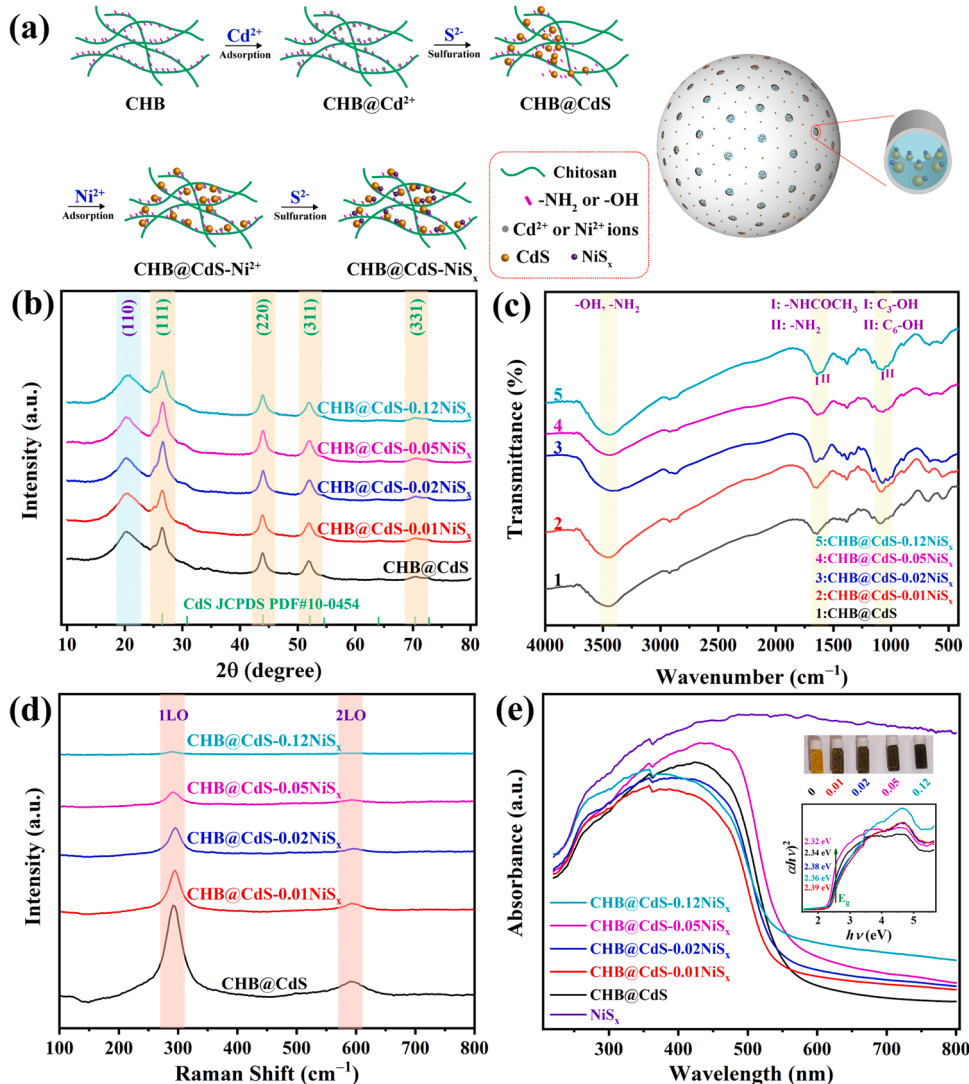


Fig. 1. (a) Schematic diagram of preparation process, (b) XRD patterns, (c) FTIR spectra, (d) Raman spectra, (e) UV-vis diffuse reflection spectra of CHB@CdS-NiS_x serial samples. The inset in (e) was Tauc plots.

3. Results and discussion

3.1. Sample characterization

The schematic diagram of material preparation was shown in Fig. 1a, because the chitosan hydrogel beads (CHB) has abundant functional

groups of $-\text{NH}_2$ and $-\text{OH}$ [41,42], Cd^{2+} -loaded precursor ($\text{CHB}@\text{Cd}^{2+}$) can be obtained by adsorption of Cd^{2+} ions to these functional groups. Subsequently, $\text{CHB}@\text{Cd}^{2+}$ reacted rapidly with Na_2S solution, the $\text{Cd}-\text{N}$ and $\text{Cd}-\text{O}$ bonds in the $\text{CHB}@\text{Cd}^{2+}$ precursor were replaced by the $\text{Cd}-\text{S}$ due to fact that the soft acid Cd^{2+} is more likely to bind to the soft base S^{2-} than the hard base characteristic $-\text{NH}_2$ and $-\text{OH}$ according to the

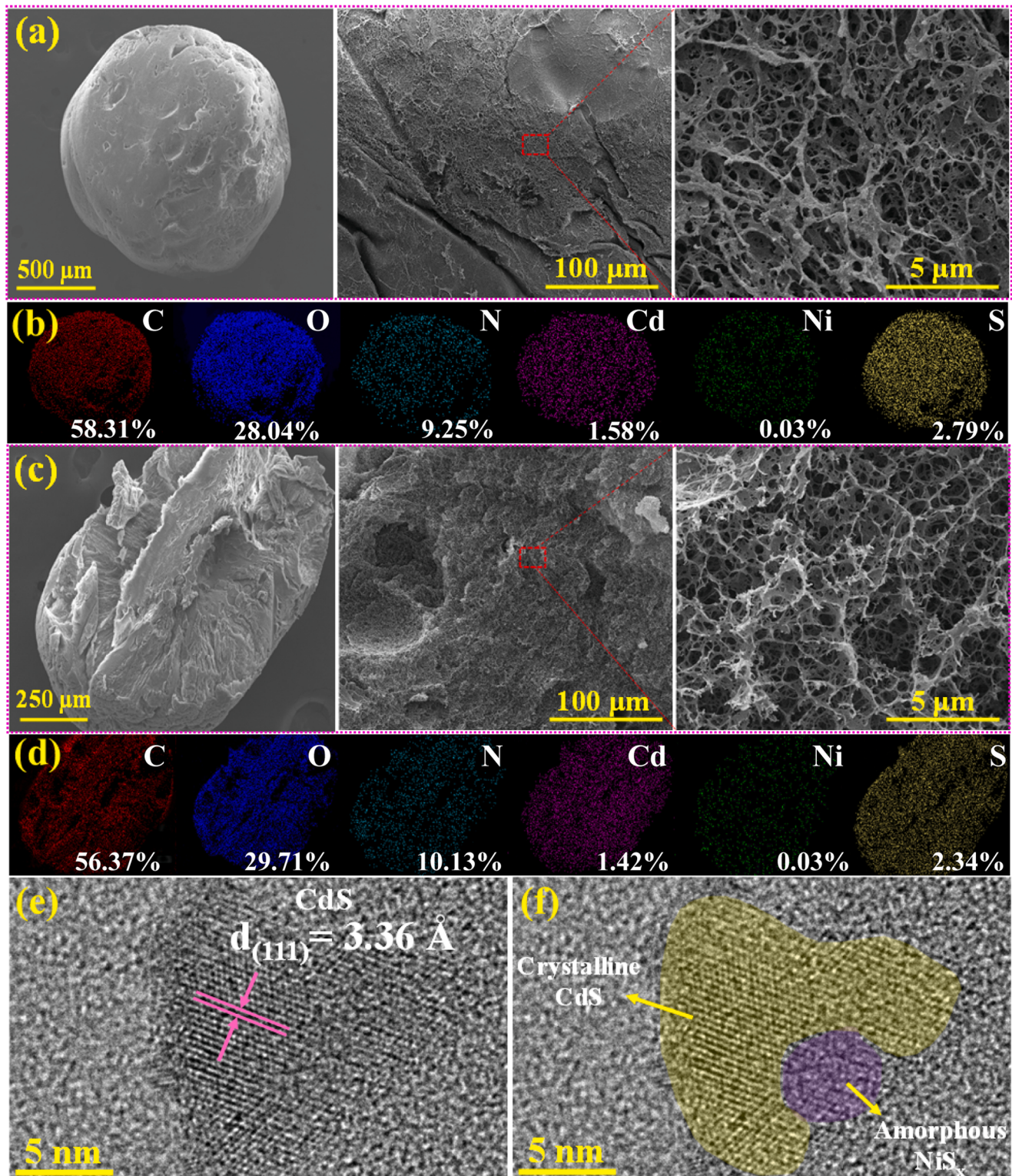


Fig. 2. (a) SEM images of the surface of $\text{CHB}@\text{CdS}-0.02\text{NiS}_x$, (b) EDS elements mapping scanning for C, O, N, Cd, Ni and S on the surface of $\text{CHB}@\text{CdS}-0.02\text{NiS}_x$, (c) SEM images of the cross-section of $\text{CHB}@\text{CdS}-0.02\text{NiS}_x$, (d) EDS elements mapping scanning for C, O, N, Cd, Ni and S on the cross-section of $\text{CHB}@\text{CdS}-0.02\text{NiS}_x$, (e) high-resolution TEM image of $\text{CHB}@\text{CdS}-0.02\text{NiS}_x$, (f) marked crystal phase and amorphous phase.

theory of hard and soft acids and bases [43], which ultimately caused the CdS *in situ* formed on CHB, *i.e.* CHB@CdS. The CHB@CdS further adsorbed Ni²⁺ through the coordination effect of –NH₂ and –OH from chitosan to obtain CHB@CdS-Ni²⁺, then it reacted with Na₂S solution to produce CHB@CdS-NiS_x. The appearance of CHB@CdS-NiS_x was a millimeter-sized hydrogel beads with a diameter of 1.8 ± 0.2 mm.

Fig. 1b shows the XRD patterns of the synthesized serial samples. For CHB@CdS, there were five characteristic diffraction peaks at 20.2°, 26.6°, 43.9°, 52.0° and 70.4° corresponding to (110) of chitosan [44] and (111), (220), (311), (331) of cubic phase CdS (JCPDS PDF#10-0454), respectively. When NiS_x with different content was grown *in situ* on the CHB@CdS, no new diffraction peaks were observed in the XRD patterns of CHB@CdS-NiS, which indicated that NiS_x existed as amorphous phase. The crystallinity of NiS was related to the synthesis method, especially the temperature and pressure [18,19]. Because the nucleation and growth process of NiS_x on CHB@CdS were carried out at room temperature and atmospheric pressure in this study, so the initial NiS_x seeds could not grow further but stay in the initial stage of amorphous NiS_x nanoparticles.

The functional group information of a series of samples was determined by FTIR. As shown in Fig. 1c, the absorption peak at about 3463.3 cm⁻¹ was caused by the stretching vibration of –NH₂ and –OH, peak at 1658.1 cm⁻¹ was the stretching vibration of C=O in the residual acetyl group (–NHCOCH₃) from chitosan, and 1600.4 cm⁻¹ is the bending vibration peak of N-H in –NH₂ [45]. In addition, 1069.6 cm⁻¹ and 1018.2 cm⁻¹ belonged to C₃–OH and C₆–OH stretching vibrations of chitosan, respectively [45]. The above results showed that chitosan existed in a series of CHB@CdS-NiS. Since the contents of CdS and NiS_x were much lower than that of chitosan (Fig. 2b and d), the relevant characteristic absorption bands were not detected in the FTIR spectra.

Raman spectra is a kind of local measurement method which is sensitive to the detection of crystallinity and microstructure of materials. Fig. 1d shows Raman spectra of CHB@CdS and serial CHB@CdS-NiS_x with the λ_{ex} = 532 nm. For CHB@CdS, the first (1LO) and the second-order longitudinal optical (2LO) phonon peaks of the cubic phase CdS were displayed at approximately 300 cm⁻¹ and 600 cm⁻¹, respectively [46]. For CHB@CdS-NiS_x, with the increase of NiS_x content, the corresponding peak intensity of 1LO and 2LO decreased gradually. It is pointed out that the peak intensity of Raman spectrum was generally related to the crystallinity of the material [33,47], the lower the crystallinity of the material, the weaker the peak intensity is. Based on this, we could come to the conclusion that amorphous NiS_x was formed in CHB@CdS-NiS_x.

The UV-vis absorption spectra were shown in Fig. 1e. Obviously, with the increased of NiS_x content, the absorbance of the samples increased in the visible light range of 600–800 nm, which was due to the excellent optical absorption properties of NiS_x. The embedded photo showed that the color of the series of CHB@CdS-NiS_x changed with the content of NiS_x. As the content of NiS_x increased, the initial yellow turned dark green and finally black. In addition, according to Kubelka-Munk equation (Text S3 in the Supplementary Material), the bandgap energies of serial samples were calculated, as shown in inset of Fig. 1e. After loading NiS_x, the bandgap energies of the CHB@CdS-NiS_x did not change significantly, both E_g value was between 2.32 and 2.39 eV. This indicated that the *in-situ* growth of NiS_x on CHB@CdS had no significant effect on the band structure of CdS [23].

As a millimeter-scale photocatalyst (*e.g.*, CHB@CdS-0.02NiS_x), photocatalytic H₂ evolution reaction not only takes place on the surface of the photocatalyst but also may take place inside the photocatalyst. Therefore, H₂ evolution performance may be affected by surface and internal microstructure of photocatalyst. The surface and cross-section morphologies of the representative CHB@CdS-0.02NiS_x were observed by scanning electron microscopy (SEM), which were shown in Fig. 2a and c, respectively. By continuously magnifying the surface of the CHB@CdS-0.02NiS_x, it can be observed that there were interlocking network macropores on its surface (Fig. 2a). At the same time, a similar

macroporous structure was also observed on the cross-section of CHB@CdS-0.02NiS_x (Fig. 2c). CHB@CdS-0.02NiS_x was a hydrogel material filled with a large amount of water. The moisture content of CHB@CdS-0.02NiS_x was as high as 95.5% determined by drying at 80 °C for 24 h to constant weight. This large amount of water inside the CHB@CdS-0.02NiS_x shaped the well-developed macroporous channels. In order to further understand the pore structure information of CHB@CdS-0.02NiS_x, the BJH pore size distribution based on the N₂ adsorption-desorption curve (Fig. S1a) and mercury intrusion porosimetry (Fig. S1b) were obtained. There were plenty of mesopores and macropores distributed in CHB@CdS-0.02NiS_x, which was basically consistent with the pore structure information observed by SEM. The abundant macropores on the surface facilitate the entry of incident light and liquid media from the surface of CHB@CdS-0.02NiS_x into its interior [48,49], and interpenetrating macroporous structure could promote multiple reflections of light in the interior, thus not only improving the utilization of incident light, but also making the internal active sites more effective use.

The elemental distribution on the surface (Fig. 2b) and cross-section (Fig. 2d) of CHB@CdS-0.02NiS_x were analyzed by SEM-EDS. Chitosan is the main component of the CHB@CdS-0.02NiS_x, the sum of C, N and O atoms on the surface and cross section accounts for 95.6% and 96.2%, respectively. The atomic ratios of Ni to Cd on the surface and cross-section of CHB@CdS-0.02NiS_x were about 0.019 and 0.021, respectively, which were close to the values measured by ICP-OES. From the surface (Fig. 2b) and cross-section (Fig. 2d) elements (Cd, Ni and S) mapping as well as radial element scanning (Fig. S2), NiS_x and CdS were uniformly distributed in the CHB.

In order to study the micromorphology of CdS and NiS_x in CHB, the CHB@CdS-0.02NiS_x were ground into powder for TEM characterization. As can be seen from Fig. S3, the particle size of CdS was about 10 nm. The corresponding high-resolution TEM (HRTEM) images were shown in Figs. 2e and S4. The lattice fringes present was attributed to the (111) crystal plane of cubic phase CdS. Due to the presence of amorphous NiS_x, the lattice fringes associated with NiS_x were not observed, which was consistent with the results of previous studies [14]. As shown in Fig. 2f, the CdS and NiS_x in Fig. 2e were marked with regions of different colors to reflect more intuitively its location distribution, NiS_x was distributed on the edge of CdS and formed an intimate interface contact with NiS_x, which is conducive to the migration and separation of photogenerated carriers at the interface. The high angle annular dark field-scanning transmission electron microscope (HAADF-STEM) image of CHB@CdS-0.02NiS_x and the corresponding element mapping were shown in Fig. S5. The distribution of elements confirmed that the irregular CdS nanoparticles and NiS_x were well dispersed on chitosan.

XPS survey spectra analysis was performed on the series of CHB@CdS-NiS_x (Fig. 3a), all elements (C, N, O, S, Ni, and Cd) in the series of samples can be detected. For S 2p (Fig. 3b), it showed two peaks at 161.0 eV and 162.4 eV, respectively, representing S 2p_{3/2} and S 2p_{1/2} of sulfide [50], and S 2p moved 0.2 eV towards high binding energy for CHB@CdS-0.02NiS_x. The Cd 3d high-resolution XPS spectra of CHB@CdS was shown in Fig. 3c. Two characteristic peaks appeared at the binding energies of 404.4 eV and 411.2 eV, which were attributed to Cd 3d_{3/2} and Cd 3d_{1/2} in CdS [51], respectively. After loading NiS_x, the Cd 3d in CHB@CdS-0.02NiS_x also moved 0.2 eV in the direction of high binding energy. The binding energies of Cd 3d and S 2p after loading NiS_x were slightly higher than that of pure CdS, indicating that the electron cloud density around Cd and S atoms decreased after deposition of NiS_x. This may be due to interface interaction caused by intimate interface contact between CdS and NiS_x [24], after all, the interface between NiS_x and CdS could be more readily formed due to the common S²⁻ for each other. In addition, Fig. 3d shows Ni 2p high-resolution XPS spectra with peaks at 855.7 eV and 873.8 eV corresponded to Ni 2p_{3/2} and Ni 2p_{1/2} in NiS_x, respectively, and 862.0 eV and 880.3 eV corresponded to the satellite peaks of Ni 2p_{3/2} and Ni 2p_{1/2}, respectively [26].

It is worth noting that there were two extra S 2p characteristic peaks

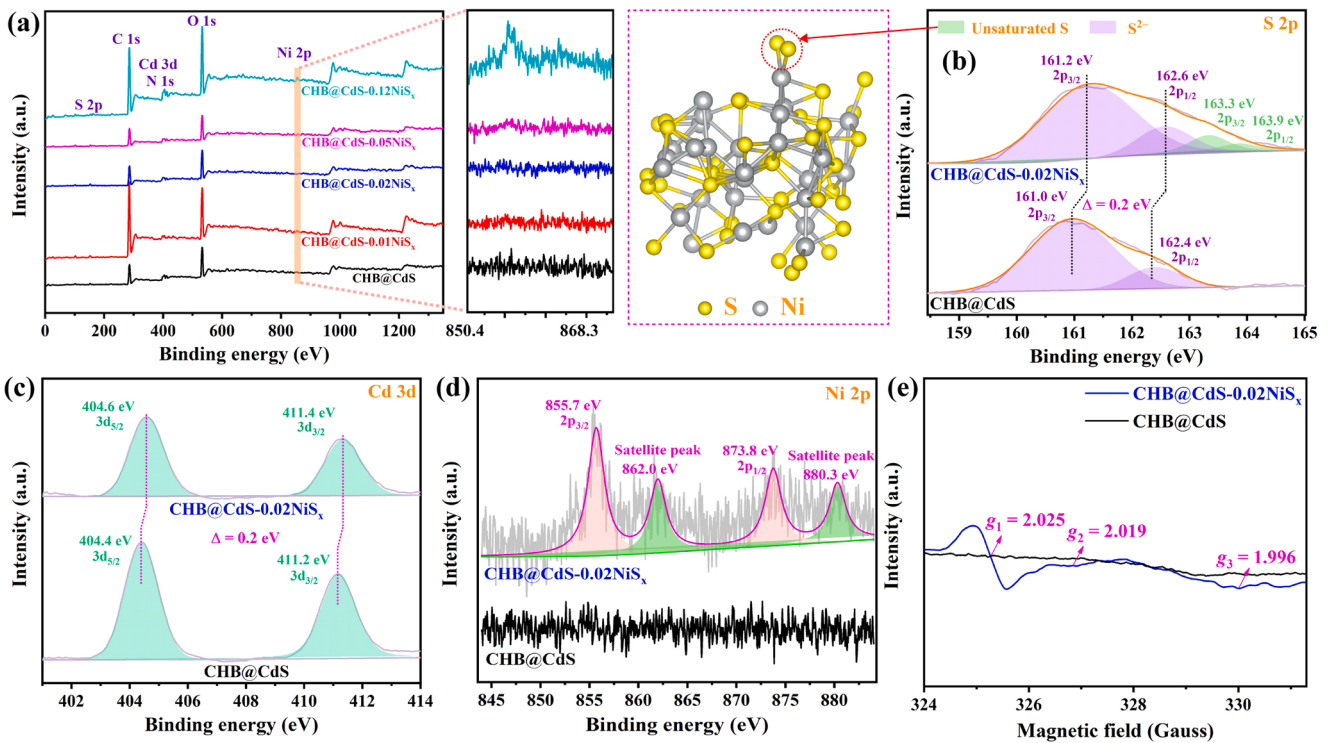


Fig. 3. (a) The XPS survey spectra of series samples, (b) S 2p, (c) Cd 3d, (d) Ni 2p XPS spectra of CHB@CdS and CHB@CdS-0.02NiS_x, (e) EPR spectra of CHB@CdS and CHB@CdS-0.02NiS_x.

in CHB@CdS-NiS_x (Fig. 3b), which were attributed to the unsaturated S site in NiS_x [52,53]. It can be further confirmed by electron paramagnetic resonance (EPR) characterization. EPR is an important tool for studying the state of unpaired electrons in materials. The signal from EPR can reflect the unsaturated coordinated atoms. In the EPR spectra of Fig. 3e, there was no EPR signal in CHB@CdS, but a group of signal

peaks appeared at $g_1 = 2.025$, $g_2 = 2.019$, and $g_3 = 1.996$ after growing NiS_x, which were attributed to the unsaturated S site in NiS_x [53]. Previous studies have pointed out that in the process of photocatalytic water splitting to produce hydrogen, the unsaturated S sites in transition metal sulfides can serve as active sites for enriching hydrogen protons [14,54,55], which will be further proved theoretically and

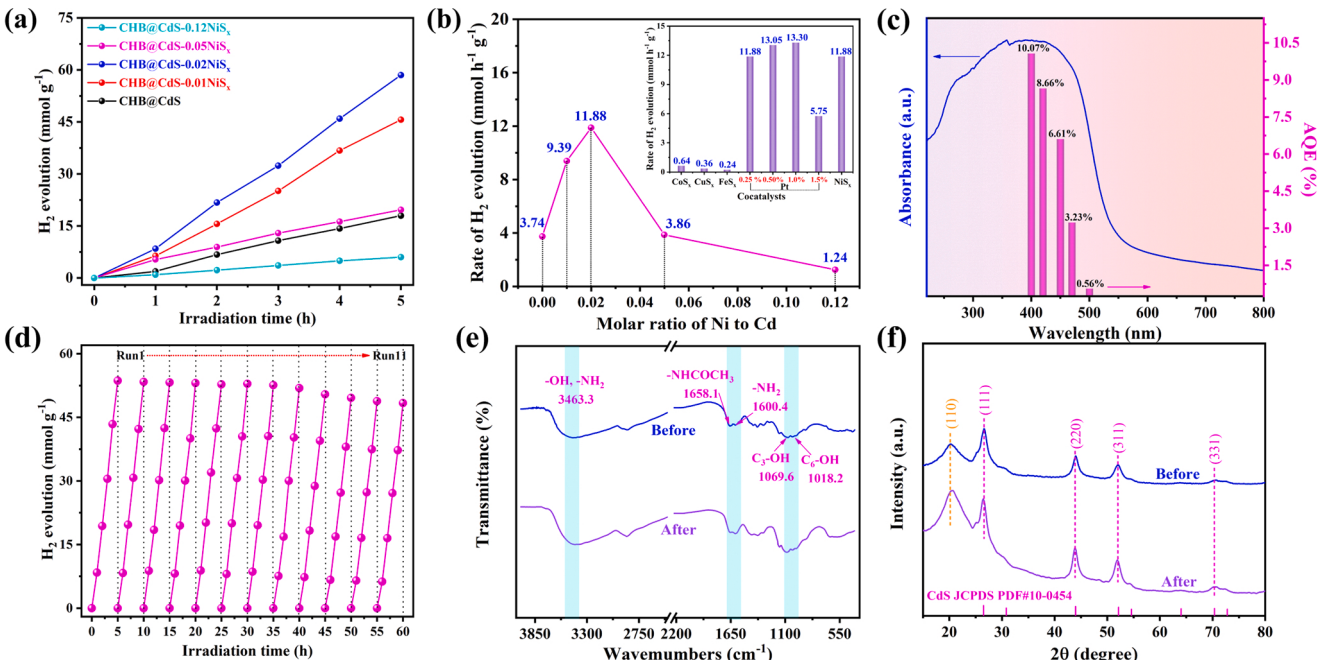


Fig. 4. (a) Effect of molar ratio of Ni to Cd on hydrogen production, (b) the variation of hydrogen production rate with the molar ratio of Ni and Cd, and comparison of hydrogen production performance between other cocatalysts and NiS_x was shown in the inset, (c) AQE measured at different single wavelengths of 400 nm, 420 nm, 450 nm, 470, and 500 nm, (d) cycle performance stability for hydrogen production over CHB@CdS-0.02NiS_x, (e) FTIR spectra and (f) XRD patterns before and after the H₂ evolution over CHB@CdS-0.02NiS_x.

experimentally in this study.

3.2. Photocatalytic hydrogen evolution performance

In order to evaluate the photocatalytic activity of the prepared photocatalyst, 0.35 mol/L Na₂S and 0.25 mol/L Na₂SO₃ were used as hole scavenger, and the hydrogen production of CHB@CdS-NiS_x with different molar ratios of Ni and Cd was measured under visible light irradiation. The amount of hydrogen varied with time as shown in Fig. 4a. The hydrogen production of all CHB@CdS-NiS_x showed a roughly linear trend. For CHB@CdS, the hydrogen production performance was 3.74 mmol/h/g. When there was a small amount of NiS_x (Ni: Cd = 0.01 or 0.02), the hydrogen production performance increased significantly. Among them, CHB@CdS-0.02NiS_x had the highest hydrogen production performance, which could reach 11.88 mmol/h/g (Fig. 4b), which is better than the hydrogen production performance of some CdS-NiS based photocatalysts previously reported (Table S1). This indicated that the introduction of NiS_x could effectively collect photogenerated electrons to promote the separation of carriers of CdS, thereby enhancing the hydrogen production performance. Further augment the content of NiS_x (Ni:Cd = 0.05 or 0.12), the performance of CHB@CdS-0.05NiS_x and CHB@CdS-0.12NiS_x were significantly reduced, which can be attributed to shielding the absorption of incident light for CdS with excessive NiS_x [18,56].

In order to highlight the advantages of NiS_x as a cocatalyst for hydrogen production of CHB@CdS, other transition metal sulfides, including CoS_x, CuS_x, and FeS_x, were *in situ* deposited on the surface of CHB@CdS according to the same method. The hydrogen production performance was shown in the inset of Figs. 4b and S6. It showed that these cocatalysts had a significant inhibitory effect on hydrogen production and were not suitable for use as cocatalyst of CHB@CdS. The noble metal Pt is a widely reported cocatalyst for hydrogen production. Pt-loaded CHB@CdS with different mass fractions (0.25 wt%, 0.50 wt%, 1.0 wt%, and 1.5 wt%) were prepared by the photo-deposition method. The results showed that the hydrogen production performance of NiS_x as a co-catalyst was comparable to that of Pt (11.88 mmol/h/g vs. 13.30 mmol/h/g). In addition, the apparent quantum efficiency (AQE) of CHB@CdS-0.02NiS_x was measured using different band-pass filters. As shown in Fig. 4c, with the increase of wavelength, AQE significantly decreased, and the variation trend was very consistent with UV-vis absorption curve, indicating that the hydrogen production was a process driven by light irradiation.

The performance of CHB@CdS-0.02NiS_x was evaluated for 11 cycles of cumulative 60 h. As shown in Fig. 4d, the performance of the first 7 cycles decreased by only 3.9% and maintained 90.0% of the initial performance after 11 cycles, indicating good performance stability. In order to understand the structural stability of the CHB@CdS-0.02NiS_x, the materials before and after hydrogen production were characterized by FTIR and XRD. Functional groups (*e.g.* -NH₂ and -OH) on chitosan did not change significantly before and after hydrogen production (Fig. 4e). The crystal faces associated with CdS and chitosan were still retained after hydrogen production, and no other impurity peaks appeared after hydrogen production (Fig. 4f), indicating that CHB@CdS-0.02NiS_x has good structural stability. Finally, Cd²⁺ and Ni²⁺ in the solution after hydrogen evolution were determined by an ICP-OES. The measured results showed that Cd²⁺ was not detected, and the concentration of Ni²⁺ was only 0.014 mg/L (equivalent to releasing 0.16 wt% of Ni element from NiS_x), which revealed that the photocorrosion of CdS was effectively inhibited and the structural damage of NiS_x in the CHB@CdS-0.02NiS_x during hydrogen evolution was negligible. And, XPS characterization analysis of CHB@CdS-0.02NiS_x before and after hydrogen evolution could further confirm the durability of the NiS_x structure (Fig. S7). In addition, our earlier research showed the photogenerated holes could be attracted by the electron-rich microenvironment induced by -NH₂ and -OH on the chitosan, which can guide the directional migration of photogenerated holes to the highest occupied

molecular orbital (HOMO) of chitosan and then be rapidly consumed by the hole scavenger [43], thus effectively promoting the photostability of CHB@CdS-0.02NiS_x.

3.3. Study on carriers separation and migration behavior

In order to study the separation behavior of photogenerated carriers of the serial samples of CHB@CdS-NiS_x, the photoluminescence (PL) spectra of the CHB@CdS-NiS_x were shown in Fig. 5a. The emission peak at 400–415 nm was attributed to the recombination of carriers from near band edge, while the emission peak at 520–535 nm was the deep level defects induced emission peak [57]. It is well known that the stronger the PL intensity, the higher the recombination level of photogenerated electrons and holes [58,59]. Obviously, compared with other materials, CHB@CdS-0.02NiS_x showed the lowest PL intensity at about 415 nm, indicating that the recombination of photogenerated carriers of CdS was suppressed by NiS_x. Time-resolved PL decay tests were further performed on CHB@CdS and CHB@CdS-0.02NiS_x (Fig. 5b). The average life of the photogenerated carriers was shortened from 2.38 ns of CHB@CdS to 2.25 ns of CHB@CdS-0.02NiS_x, which signified the rapid migration of the photogenerated electrons from CdS to NiS_x [60,61]. The separation behavior of photogenerated carriers can be further revealed by photoelectrochemical measurements. As shown in Fig. 5c, CHB@CdS-0.02NiS_x showed significantly increased photocurrent density, further demonstrating that NiS_x can effectively promote separation of photoinduced carriers. In addition, the electrochemical impedance spectroscopy (EIS) and its corresponding equivalent circuit model (inset) were shown in Fig. 5d, where R_s is the solution resistance, R_{ct} is the charge transfer resistance of the electrode/electrolyte interface, and CPE is the constant capacitance phase element in the bulk [62]. The fitted equivalent circuit elements from the EIS data were summarized in Table S2. The fitted value of the R_{ct} was dropped from 44,880 kΩ cm⁻² for CHB@CdS to 1794 kΩ cm⁻² for CHB@CdS-0.02NiS_x, revealing that the CHB@CdS with the optimum NiS_x content had a lower interfacial transfer resistance than those of other samples to accelerate carrier separation, thereby improving the performance of hydrogen production.

Kelvin probe force microscopy (KPFM) detection was performed to visualize the charge transfer in CHB@CdS-0.02NiS_x. AFM topography (Fig. 5e) shows NiS_x distribution along the edge of CdS. However, a clear contrast difference can be observed in the Kelvin potential image under dark (Fig. 5f) and light (Fig. 5g) irradiation conditions. The lower potential region at the edge of the contour was the NiS_x, while the higher potential region in the middle belonged to the CdS. A line scan analysis, Fig. 5h, reveals decline in the Kelvin potential of *ca.* 53.7 mV at a marked location A (NiS_x) and rise potential of *ca.* 43.7 mV at a marked location B (CdS), indicating the photo-induced electrons transfer from CdS to NiS_x.

3.4. Mechanism analysis of photocatalytic hydrogen evolution

Work function is an important physical parameter in the study of charge transfer between semiconductor photocatalysts and cocatalysts. In order to theoretically explain the above experimental results, the work function of CdS and NiS_x was calculated by density functional theory (DFT). The choice of crystal face is crucial to the calculation of work function. From the above XRD patterns (Fig. 1b), the dominant crystal face exposed by cubic phase CdS in the CHB@CdS-0.02NiS_x was the (111) crystal face. The variation of electrostatic potential of CdS (111) facet along the Z-axis was shown in Fig. 6a. The work function (Φ) is numerically equal to the difference between the vacuum level and the Fermi level, so the work function of CdS (111) facet was 4.00 eV [63]. The variation of electrostatic potential of isotropic NiS_x along the Z-axis was shown in Fig. 6b and its work function was 5.19 eV. CdS had a smaller work function than NiS_x, indicating that CdS had a higher Fermi level than NiS_x, which promoted the migration of photogenerated electrons from CdS to NiS_x. And for the convenience of comparison, the

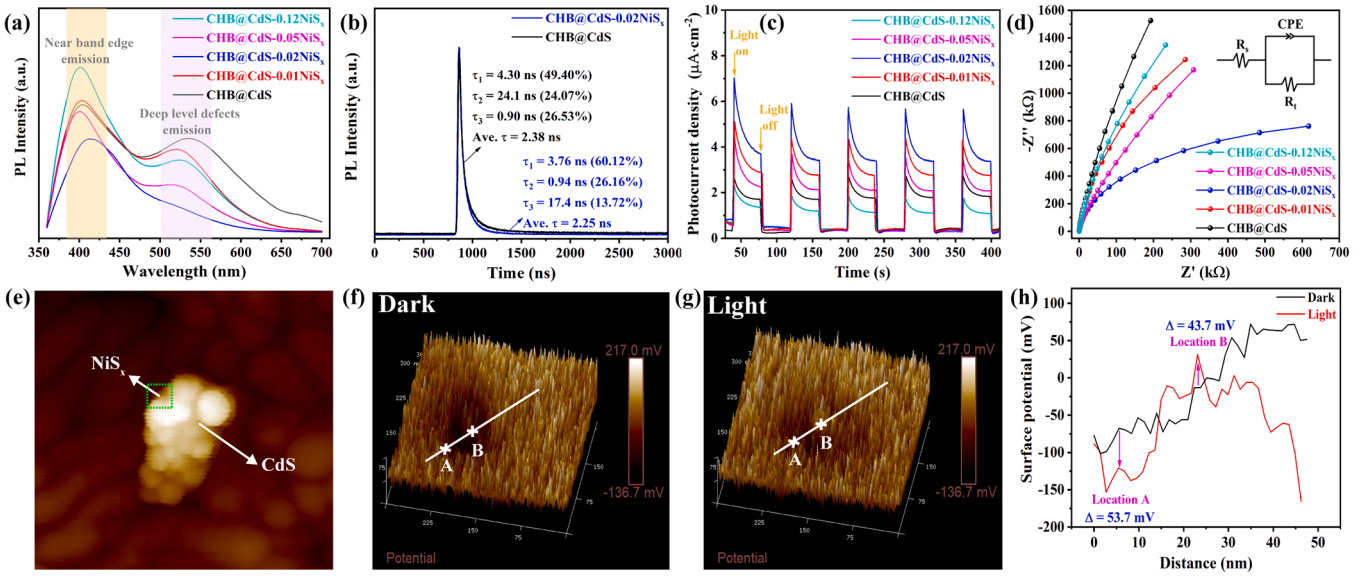


Fig. 5. (a) Photoluminescence spectra of serial samples, (b) time-resolved PL decay curves of the CHB@CdS and CHB@CdS-0.02NiS_x, (c) transient photocurrent response and (d) EIS analysis of serial samples, (e) 2D topography image for CHB@CdS-0.02NiS_x, (f) Kelvin potential image under dark condition, (g) Kelvin potential image under light condition, (h) line profiles of Kelvin potential extracted from the potential images of dark and light conditions.

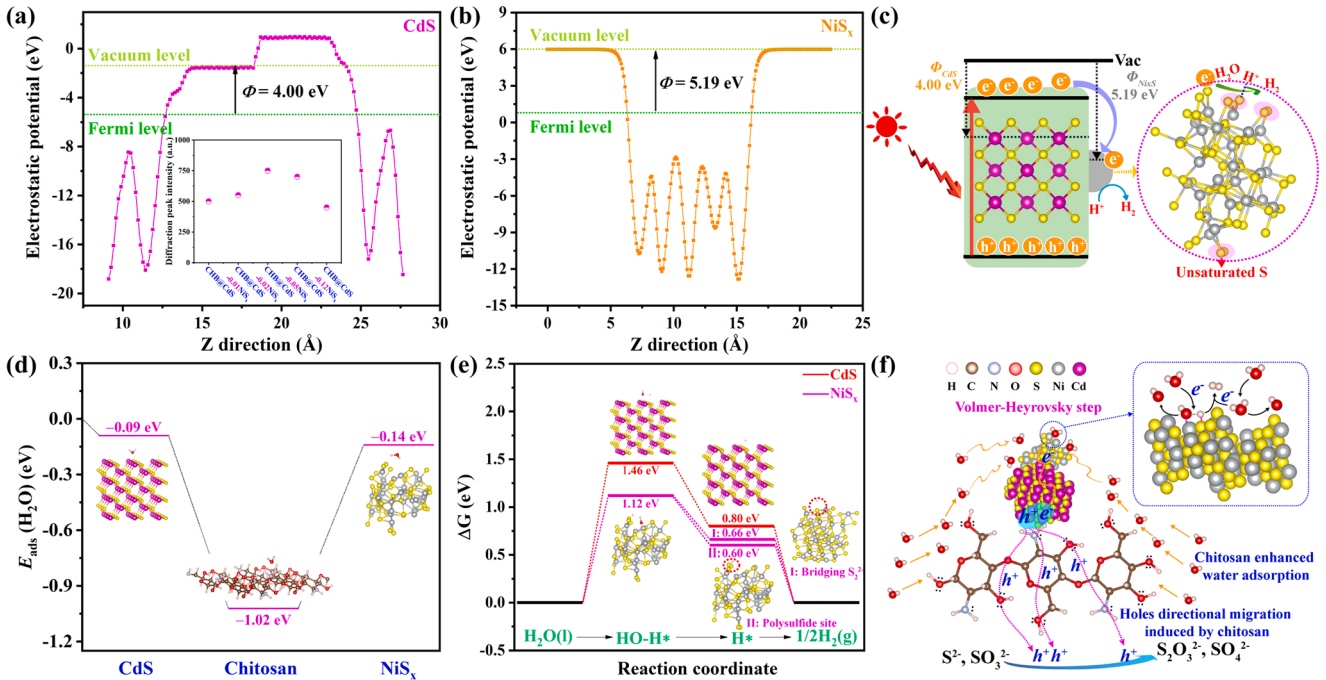


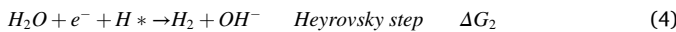
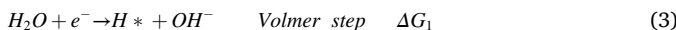
Fig. 6. Calculated work function of (a) CdS and (b) NiS_x, the effect of molar ratio of Ni to Cd on the diffraction peak intensity of CdS (111) was shown in the inset of (a); (c) schematic diagram of photoinduced carriers migration and hydrogen evolution on the CdS-NiS_x, (d) adsorption energies of chitosan, CdS, and NiS_x to H₂O, (e) Gibbs free energy diagrams for the H₂ evolution pathway on the CdS and NiS_x, (f) schematic diagram of mechanism for photocatalytic hydrogen evolution on the CHB@CdS-NiS_x.

work function of the crystalline phase NiS (102) was also investigated in Fig. S8. The work function of NiS_x (5.19 eV) was greater than that of NiS (5.05 eV), indicating greater driving force for electrons migration from CdS to NiS_x. Previous studies have revealed that the CdS (111) facet is a polar facet, in which the photogenerated electrons and holes are exclusively localized distributed on the Cd and S layers, respectively, rendering separation for photogenerated carriers [64]. The diffraction peak intensity of the CdS (111) facet varied with the molar ratio of Ni to Cd as shown in the inset of Fig. 6a, the NiS_x content affected the exposure of CdS (111) facet, when the molar ratio of Ni to Cd was 0.02 (*i.e.*,

CHB@CdS-0.02NiS_x), the CdS (111) facet tended to be exposed. Therefore, the exposed polar facet of CdS (111) could promote the performance of photocatalytic H₂ evolution. In addition, due to the presence of a large amount of unsaturated S sites distributed on NiS_x, the electrons transferred from CdS to NiS_x could further move to the edge unsaturated S sites, and the protons enriched in unsaturated S sites were reduced to hydrogen (Fig. 6c).

Na₂S-Na₂SO₃ mixed solution was used as a sacrificial agent in the photocatalytic hydrogen production process in this study and the reaction solution is an alkaline media (pH ~13.39). Since the alkaline media

is scarce of protons, the adsorption and dissociation of water molecules may be the decisive step for hydrogen production [40,65,66]. In order to gain insight into this process in theory, the adsorption energies of chitosan, CdS and NiS_x to H₂O were studied based DFT. Fig. 6d shows the calculation models and adsorption energies of chitosan, CdS and NiS_x to H₂O. And, the H₂O adsorption energies of the crystalline phase NiS was also studied for comparison (Fig. S9). Chitosan exhibited a stronger adsorption effect on H₂O than that of CdS, NiS_x, and NiS by comparing the adsorption energies. Therefore, chitosan was conducive to concentrate H₂O molecules around the CdS-NiS_x photocatalyst. The H₂O concentrated around chitosan will migrate to CdS or NiS_x under the action of the concentration driving force. The H₂O adsorbed on CdS or NiS_x will carry out the dissociation of H₂O and the subsequent hydrogen adsorption/desorption process. Previous studies have shown that the H₂O dissociation and hydrogen adsorption/desorption processes on the surface of the transition metal sulfides in alkaline media usually involves the Volmer (Eq. 3)-Heyrovsky (Eq. 4) reaction pathway [67]:



The DFT calculation results for processes of Volmer (ΔG_1)-Heyrovsky (ΔG_2) on NiS_x and CdS were shown in Figs. 6e, and S10 shows a DFT calculation result of crystalline phase NiS as a comparison. The ΔG_1 of CdS was 1.46 eV (Fig. 6e), which was the maximum, indicated that the dissociation of H₂O on CdS under alkaline conditions required a higher activation energy [68]. This process may be the cause of the sluggish hydrogen evolution reaction kinetics of pure CdS. For NiS_x, the ΔG_1 was the smallest, signifying that NiS_x loaded on CHB@CdS could reduce the activation energy of H₂O dissociation [68,69]. In addition, the ΔG_2 of bridging S₂²⁻ and polysulfide sites on the edge of NiS_x related to hydrogen absorption/desorption was smaller than that of CdS (Fig. 6e), suggesting that the reduction process of protons to generate H₂ on NiS_x was more energetically feasible and further confirmed that hydrogen production process occurred on NiS_x cocatalyst. More importantly, in the process of H₂O dissociation and hydrogen absorption/desorption, the ΔG_1 and ΔG_2 of NiS_x were both smaller than that of crystalline phase NiS, which means that, theoretically, NiS_x was more effective in the activation of H₂O molecules and the reduction of protons than crystalline phase NiS. Therefore, NiS_x was more suitable than crystalline phase NiS as a cocatalyst for CdS to boost H₂ evolution reaction.

Based on the above characterization and theoretical calculation analysis, the photocatalytic hydrogen evolution mechanism of CHB@CdS-NiS_x was proposed in Fig. 6f. The hydrogen evolution mainly includes the following three process: (I) The enrichment of electrons on active sites. Under visible light irradiation, the photoinduced electrons from valence band of CdS in CHB@CdS-NiS_x jumped to the conduction band. Due to the higher Fermi level of CdS than NiS_x, the electrons quickly flowed to NiS_x and further migrated to the edge unsaturated S sites; (II) the adsorption of protons (H⁺) on the active sites. H₂O molecules were first concentrated around CdS-NiS_x by the chitosan in CHB@CdS-NiS_x, and the H₂O molecules were further dissociated on the NiS_x to produce H⁺, then the H⁺ were adsorbed on the edge unsaturated S sites [14,55]; (III) hydrogen generation. The H⁺ adsorbed at the unsaturated S site were reduced by its enriched electrons to generate H₂. In addition, the photo-generated holes from CdS were attracted by the electron-rich microenvironment induced by -NH₂ and -OH on the chitosan, which can guide the directional migration of photogenerated holes and then be rapidly consumed by the hole scavenger [43], ultimately effectively promoting the photostability of CHB@CdS-0.02NiS_x and resulting in the enhancement of hydrogen production performance.

4. Conclusions

In summary, we reported highly active CdS-NiS_x photocatalyst-cocatalyst system confined growth inside the hydrophilic chitosan

hydrogel beads (CHB@CdS-NiS_x). NiS_x was uniformly dispersed on the surface of CdS, forming an intimate interface contact to accelerate the electron migration from CdS to NiS_x. Owing to irregular loose structure, NiS_x possessed abundant unsaturated edge active S as H₂-evolution sites to facilitate performance of hydrogen production. The hydrogen production performance of CHB@CdS-0.02NiS_x was the highest (11.88 mmol/h/g) and still maintain 90.0% initial performance after the cumulative 60 h for 11 cycles. As investigated using DFT calculation, activation energy of H⁺•OH in water was reduced veritably on the sites of NiS_x, which promoted the dissociation of water and optimized both of adsorption and desorption of hydrogen generation, revealing that its hydrogen evolution pathway (H₂O → H⁺ → H₂) was more energetically feasible. This work provides new ideas for cleverly constructing low-cost, high-efficiency and durable amorphous co-catalysts of transition metal sulfides to realize the efficient conversion of solar energy to hydrogen energy.

CRediT authorship contribution statement

Tao Yu established the research line and supervised the current work; Xin Tan co-supervised the current work; Yizhong Zhang performed the experiments, data analysis and wrote the manuscript; Wei Zhou: theoretical calculations; Lequan Liu, Huaiyuan Wang, and Jinhua Ye: resources; Yuan Tang, Yuchen Guo, and Zikang Geng were involved in the analysis of data and revised the manuscript. All the authors reviewed, approved, and contributed to the final version of the manuscript.

Declaration of Competing Interest

The authors declare that they have no known competing financial interests or personal relationships that could have appeared to influence the work reported in this paper.

Acknowledgments

This work was supported by the National Key Research and Development Program of China (2021YFA1500700) and the National Natural Science Foundation of China (22066022).

Appendix A. Supplementary material

Supplementary material (e.g., the preparation method of CHB@CdS containing CoSx, CuSx, and FeSx, the methods of photoelectrochemical measurements, comparison of hydrogen production activity of CdS/NiS-related photocatalysts, BJH pore size distribution of CHB@CdS-0.02NiS_x, mercury intrusion pore size distribution of CHB@CdS-0.02NiS_x, optimization of cocatalysts (CoSx, CuSx and FeSx) amount, XPS characterization of CHB@CdS-0.02NiS_x before and after hydrogen evolution, calculated work function of crystalline phase NiS, and Gibbs free energy diagrams for the H₂ evolution pathway on crystalline phase NiS) is available.

Appendix B. Supporting information

Supplementary data associated with this article can be found in the online version at doi:10.1016/j.apcatb.2021.121055.

References

- [1] T. Takata, J. Jiang, Y. Sakata, M. Nakabayashi, N. Shibata, V. Nandal, K. Seki, T. Hisatomi, K. Domen, Photocatalytic water splitting with a quantum efficiency of almost unity, *Nature* 581 (2020) 411–414.
- [2] H. Nishiyama, T. Yamada, M. Nakabayashi, Y. Maehara, M. Yamaguchi, Y. Kuromiya, H. Tokudome, S. Akiyama, T. Watanabe, R. Narushima, S. Okunaka, N. Shibata, T. Takata, T. Hisatomi, K. Domen, Photocatalytic solar hydrogen production from water on a 100 m²-scale, *Nature* 598 (2021) 304–307.

- [3] Q. Zhao, Y. Li, K. Hu, X. Guo, Y. Qu, Z. Li, F. Yang, H. Liu, C. Qin, L. Jing, Controlled synthesis of nitro-terminated poly[2-(3-thienyl)-ethanol]/g-C₃N₄ nanosheet heterojunctions for efficient visible-light photocatalytic hydrogen evolution, *ACS Sustain. Chem. Eng.* 9 (2021) 7306–7317.
- [4] Z. Wang, C. Li, K. Domen, Recent developments in heterogeneous photocatalysts for solar-driven overall water splitting, *Chem. Soc. Rev.* 48 (2019) 2109–2125.
- [5] X. Zhang, P. Zhai, Y. Zhang, Y. Wu, C. Wang, L. Ran, J. Gao, Z. Li, B. Zhang, Z. Fan, L. Sun, J. Hou, Engineering single-atomic Ni-N₄O sites on semiconductor photoanodes for high-performance photoelectrochemical water splitting, *J. Am. Chem. Soc.* (2021), <https://doi.org/10.1021/jacs.1c07391>.
- [6] J.A. Nasir, Zu Rehman, S.N.A. Shah, A. Khan, I.S. Butler, C.R.A. Catlow, Recent developments and perspectives in CdS-based photocatalysts for water splitting, *J. Mater. Chem. A* 8 (2020) 20752–20780.
- [7] Y.-J. Yuan, D. Chen, Z.-T. Yu, Z.-G. Zou, Cadmium sulfide-based nanomaterials for photocatalytic hydrogen production, *J. Mater. Chem. A* 6 (2018) 11606–11630.
- [8] D. Zhao, C.-F. Yang, Recent advances in the TiO₂/CdS nanocomposite used for photocatalytic hydrogen production and quantum-dot-sensitized solar cells, *Renew. Sust. Energy Rev.* 54 (2016) 1048–1059.
- [9] S. Chen, D. Huang, P. Xu, W. Xue, L. Lei, M. Cheng, R. Wang, X. Liu, R. Deng, Semiconductor-based photocatalysts for photocatalytic and photoelectrochemical water splitting: will we stop with photocorrosion? *J. Mater. Chem. A* 8 (2020) 2286–2322.
- [10] J. Ran, J. Zhang, J. Yu, M. Jaroniec, S.Z. Qiao, Earth-abundant cocatalysts for semiconductor-based photocatalytic water splitting, *Chem. Soc. Rev.* 43 (2014) 7787–7812.
- [11] J. Liu, Y. Li, X. Zhou, H. Jiang, H.G. Yang, C. Li, Positively charged Pt-based cocatalysts: an orientation for achieving efficient photocatalytic water splitting, *J. Mater. Chem. A* 8 (2020) 17–26.
- [12] Q. Wang, J. Li, N. An, Y. Bai, X. Lu, J. Li, H. Ma, R. Wang, F. Wang, Z. Lei, W. Shangguan, Preparation of a novel recyclable cocatalyst wool–Pd for enhancement of photocatalytic H₂ evolution on CdS, *Int. J. Hydrog. Energy* 38 (2013) 10761–10767.
- [13] P. Wang, Y. Sheng, F. Wang, H. Yu, Synergistic effect of electron-transfer mediator and interfacial catalytic active-site for the enhanced H₂-evolution performance: a case study of CdS-Au photocatalyst, *Appl. Catal. B-Environ.* 220 (2018) 561–569.
- [14] W. Zhong, X. Wu, Y. Liu, X. Wang, J. Fan, H. Yu, Simultaneous realization of sulfur-rich surface and amorphous nanocluster of NiS_{1+x} cocatalyst for efficient photocatalytic H₂ evolution, *Appl. Catal. B-Environ.* 280 (2021), 119455.
- [15] X. Zou, Y. Zhang, Noble metal-free hydrogen evolution catalysts for water splitting, *Chem. Soc. Rev.* 44 (2015) 5148–5180.
- [16] X. Zong, H. Yan, G. Wu, G. Ma, F. Wen, L. Wang, C. Li, Enhancement of photocatalytic H₂ evolution on CdS by loading MoS₂ as cocatalyst under visible light irradiation, *J. Am. Chem. Soc.* 130 (2008) 7176–7177.
- [17] S. Iqbal, Z. Pan, K. Zhou, Enhanced photocatalytic hydrogen evolution from in situ formation of few-layered MoS₂/CdS nanosheet-based van der Waals heterostructures, *Nanoscale* 9 (2017) 6638–6642.
- [18] W. Zhang, Y. Wang, Z. Wang, Z. Zhong, R. Xu, Highly efficient and noble metal-free NiS/CdS photocatalysts for H₂ evolution from lactic acid sacrificial solution under visible light, *Chem. Commun.* 46 (2010) 7631–7633.
- [19] J. Zhang, S.Z. Qiao, L. Qi, J. Yu, Fabrication of NiS modified CdS nanorod p–n junction photocatalysts with enhanced visible-light photocatalytic H₂-production activity, *Phys. Chem. Chem. Phys.* 15 (2013) 12088–12094.
- [20] Y. Wan, S. Du, C. Lu, K. Ren, B. Shi, S. Liu, C. Li, W. Dou, P. Fang, N. Ye, Metallic CuS decorated CdS nanowires for efficient photocatalytic H₂ evolution under visible-light irradiation, *J. Alloy. Compd.* 871 (2021), 159461.
- [21] K. Zhang, M. Fujitsuka, Y. Du, T. Majima, 2D/2D Heterostructured CdS/WS₂ with efficient charge separation improving H₂ evolution under visible light irradiation, *ACS Appl. Mater. Interfaces* 10 (2018) 20458–20466.
- [22] Y. Zhong, G. Zhao, F. Ma, Y. Wu, X. Hao, Utilizing photocorrosion-recrystallization to prepare a highly stable and efficient CdS/WS₂ nanocomposite photocatalyst for hydrogen evolution, *Appl. Catal. B-Environ.* 199 (2016) 466–472.
- [23] S. Guan, X. Fu, Y. Zhang, Z. Peng, β-NiS modified CdS nanowires for photocatalytic H₂ evolution with exceptionally high efficiency, *Chem. Sci.* 9 (2018) 1574–1585.
- [24] C. Li, H. Wang, S.B. Naghadeh, J.Z. Zhang, P. Fang, Visible light driven hydrogen evolution by photocatalytic reforming of lignin and lactic acid using one-dimensional NiS/CdS nanostructures, *Appl. Catal. B-Environ.* 227 (2018) 229–239.
- [25] Y. Zhang, Z. Peng, S. Guan, X. Fu, Novel β-NiS film modified CdS nanoflowers heterostructure nanocomposite: extraordinarily highly efficient photocatalysts for hydrogen evolution, *Appl. Catal. B-Environ.* 224 (2018) 1000–1008.
- [26] C. Zhang, B. Liu, X. Cheng, Z. Guo, T. Zhuang, Z. Lv, A CdS@NiS reinforced concrete structure derived from nickel foam for efficient visible-light H₂ production, *Chem. Eng. J.* 393 (2020), 124774.
- [27] W. Zhong, D. Gao, H. Yu, J. Fan, J. Yu, Novel amorphous NiCuS H₂-evolution cocatalyst: optimizing surface hydrogen desorption for efficient photocatalytic activity, *Chem. Eng. J.* 419 (2021), 129652.
- [28] L. Zhang, C. Lu, F. Ye, Z. Wu, Y. Wang, L. Jiang, L. Zhang, C. Cheng, Z. Sun, L. Hu, Vacancies boosting strategy enabling enhanced oxygen evolution activity in a library of novel amorphous selenite electrocatalysts, *Appl. Catal. B-Environ.* 284 (2021), 119758.
- [29] S. Sun, G. Shen, Z. Chen, L. Pan, X. Zhang, J.-J. Zou, Harvesting urbach tail energy of ultrathin amorphous nickel oxide for solar-driven overall water splitting up to 680 nm, *Appl. Catal. B-Environ.* 285 (2021), 119798.
- [30] J. He, P. Lyu, B. Jiang, S. Chang, H. Du, J. Zhu, H. Li, A novel amorphous alloy photocatalyst (NiB/In₂O₃) composite for sunlight-induced CO₂ hydrogenation to HCOOH, *Appl. Catal. B-Environ.* 298 (2021), 120603.
- [31] B. Ju, H.J. Song, H. Yoon, D.-W. Kim, Amorphous hydrated vanadium oxide with enlarged interlayer spacing for aqueous zinc-ion batteries, *Chem. Eng. J.* 420 (2021), 130528.
- [32] J. Zheng, X. Lian, M. Wu, F. Zheng, Y. Gao, H. Niu, A synergistic strategy combining amorphous Ni₃S₄ quantum dots and zeolite imidazole framework nanosheets for enhanced supercapacitor performance, *Colloid Surf. A-Physicochem. Eng. Asp.* 623 (2021), 126710.
- [33] Q. Huang, Y. Zhang, W. Zhou, X. Huang, Y. Chen, X. Tan, T. Yu, Amorphous molybdenum sulfide mediated EDTA with multiple active sites to boost heavy metal ions removal, *Chin. Chem. Lett.* 32 (2021) 2797–2802.
- [34] Y. Zhou, H.J. Fan, Progress and challenge of amorphous catalysts for electrochemical water splitting, *ACS Mater. Lett.* 3 (2020) 136–147.
- [35] B. Wang, G.M. Biesold, M. Zhang, Z. Lin, Amorphous inorganic semiconductors for the development of solar cell, photoelectrocatalytic and photocatalytic applications, *Chem. Soc. Rev.* 50 (2021) 6914–6949.
- [36] C. Guo, Y. Shi, S. Lu, Y. Yu, B. Zhang, Amorphous nanomaterials in electrocatalytic water splitting, *Chin. J. Catal.* 42 (2021) 1287–1296.
- [37] J. Wen, X. Li, H. Li, S. Ma, K. He, Y. Xu, Y. Fang, W. Liu, Q. Gao, Enhanced visible-light H₂ evolution of g-C₃N₄ photocatalysts via the synergistic effect of amorphous NiS and cheap metal-free carbon black nanoparticles as co-catalysts, *Appl. Surf. Sci.* 358 (2015) 204–212.
- [38] J. Wen, J. Xie, H. Zhang, A. Zhang, Y. Liu, X. Chen, X. Li, Constructing multifunctional metallic Ni interface layers in the g-C₃N₄ nanosheets/amorphous NiS heterojunctions for efficient photocatalytic H₂ generation, *ACS Appl. Mater. Interfaces* 9 (2017) 14031–14042.
- [39] G. Kresse, J. Hafner, *Ab initio* molecular dynamics for liquid metals, *Phys. Rev. B Condens. Matter* 47 (1993) 558–561.
- [40] J. Kim, H. Jung, S.M. Jung, J. Hwang, D.Y. Kim, N. Lee, K.S. Kim, H. Kwon, Y. T. Kim, J.W. Han, J.K. Kim, Tailoring binding abilities by incorporating oxophilic transition metals on 3D nanostructured Ni arrays for accelerated alkaline hydrogen evolution reaction, *J. Am. Chem. Soc.* 143 (2021) 1399–1408.
- [41] A.J. Varma, S.V. Deshpande, J.F. Kennedy, Metal complexation by chitosan and its derivatives: a review, *Carbohydr. Polym.* 55 (2004) 77–93.
- [42] E. Guibal, Interactions of metal ions with chitosan-based sorbents: a review, *Sep. Purif. Technol.* 38 (2004) 43–74.
- [43] Y. Zhang, W. Zhou, L. Jia, X. Tan, Y. Chen, Q. Huang, B. Shao, T. Yu, Visible light driven hydrogen evolution using external and confined CdS: effect of chitosan on carriers separation, *Appl. Catal. B-Environ.* 277 (2020), 119152.
- [44] J. Yang, J. Duan, L. Zhang, B. Lindman, H. Edlund, M. Norgren, Spherical nanocomposite particles prepared from mixed cellulose–chitosan solutions, *Cellulose* 23 (2016) 3105–3115.
- [45] Z. Li, Y. Du, Z. Zhang, D. Pang, Preparation and characterization of CdS quantum dots chitosan biocomposite, *React. Funct. Polym.* 55 (2003) 35–43.
- [46] H. Yu, W. Zhong, X. Huang, P. Wang, J. Yu, Suspensible cubic-phase CdS nanocrystal photocatalyst: facile synthesis and highly efficient H₂-evolution performance in a sulfur-rich system, *ACS Sustain. Chem. Eng.* 6 (2018) 5513–5523.
- [47] Z. Lin, C. Du, B. Yan, C. Wang, G. Yang, Two-dimensional amorphous NiO as a plasmonic photocatalyst for solar H₂ evolution, *Nat. Commun.* 9 (2018) 4036.
- [48] Y. Li, Y. Jiang, Z. Ruan, K. Lin, Z. Yu, Z. Zheng, X. Xu, Y. Yuan, Simulation-guided synthesis of graphitic carbon nitride beads with 3D interconnected and continuous meso/macropore channels for enhanced light absorption and photocatalytic performance, *J. Mater. Chem. A* 5 (2017) 21300–21312.
- [49] Y. Li, Z. Ruan, Y. He, J. Li, K. Li, Y. Jiang, X. Xu, Y. Yuan, K. Lin, *In situ*fabrication of hierarchically porous g-C₃N₄ and understanding on its enhanced photocatalytic activity based on energy absorption, *Appl. Catal. B-Environ.* 236 (2018) 64–75.
- [50] A. Meng, X. Yuan, T. Shen, J. Zhao, G. Song, Y. Lin, Z. Li, Amorphous nickel sulfide nanoparticles anchored on N-doped graphene nanotubes with superior properties for high-performance supercapacitors and efficient oxygen evolution reaction, *Nanoscale* 12 (2020) 4655–4666.
- [51] F. Quan, J. Zhang, D. Li, Y. Zhu, Y. Wang, Y. Bu, Y. Qin, Y. Xia, S. Komarneni, D. Yang, Biomass as a template leads to CdS@Carbon aerogels for efficient photocatalytic hydrogen evolution and stable photoelectrochemical cells, *ACS Sustain. Chem. Eng.* 6 (2018) 14911–14918.
- [52] K. Yu, H.-B. Huang, J.-T. Wang, G.-F. Liu, Z. Zhong, Y.-F. Li, H.-L. Cao, J. Lü, R. Cao, Engineering cation defect-mediated Z-scheme photocatalysts for a highly efficient and stable photocatalytic hydrogen production, *J. Mater. Chem. A* 9 (2021) 7759–7766.
- [53] Q. Xu, Y. Liu, H. Jiang, Y. Hu, H. Liu, C. Li, Unsaturated sulfur edge engineering of strongly coupled MoS₂ nanosheet–carbon macroporous hybrid catalyst for enhanced hydrogen generation, *Adv. Energy Mater.* 9 (2019), 1802553.
- [54] K. Chang, Z. Mei, T. Wang, Q. Kang, S. Ouyang, J. Ye, MoS₂/graphene cocatalyst for efficient photocatalytic H₂ evolution under visible light irradiation, *ACS Nano* 8 (2014) 7078–7087.
- [55] Y. Deng, L.R.L. Ting, P.H.L. Neo, Y.-J. Zhang, A.A. Peterson, B.S. Yeo, Operando Raman spectroscopy of amorphous molybdenum sulfide (MoS_x) during the electrochemical hydrogen evolution reaction: identification of sulfur atoms as catalytically active sites for H⁺ reduction, *ACS Catal.* 6 (2016) 7790–7798.
- [56] D. Huang, M. Wen, C. Zhou, Z. Li, M. Cheng, S. Chen, W. Xue, L. Lei, Y. Yang, W. Xiong, W. Wang, Zn_xCd_{1-x}S based materials for photocatalytic hydrogen evolution, pollutants degradation and carbon dioxide reduction, *Appl. Catal. B-Environ.* 267 (2020), 118651.
- [57] K. Zhang, Y. Dai, Z. Zhou, S. Ullah Jan, L. Guo, J.R. Gong, Polarization-induced saw-tooth-like potential distribution in zincblende-wurtzite superlattice for efficient charge separation, *Nano Energy* 41 (2017) 101–108.

- [58] J. Wang, T. Bo, B. Shao, Y. Zhang, L. Jia, X. Tan, W. Zhou, T. Yu, Effect of S vacancy in Cu₃SnS₄ on high selectivity and activity of photocatalytic CO₂ reduction, *Appl. Catal. B-Environ.* 297 (2021), 120498.
- [59] J. Zhang, J. Lang, Y. Wei, Q. Zheng, L. Liu, Y.-H. Hu, B. Zhou, C. Yuan, M. Long, Efficient photocatalytic H₂O₂ production from oxygen and pure water over graphitic carbon nitride decorated by oxidative red phosphorus, *Appl. Catal. B-Environ.* 298 (2021), 120522.
- [60] X. Lu, C.Y. Toe, F. Ji, W. Chen, X. Wen, R.J. Wong, J. Seidel, J. Scott, J.N. Hart, Y. H. Ng, Light-induced formation of MoO_xS_y clusters on CdS nanorods as cocatalyst for enhanced hydrogen evolution, *ACS Appl. Mater. Interfaces* 12 (2020) 8324–8332.
- [61] Z. Chen, H. Gong, Q. Liu, M. Song, C. Huang, NiSe₂ nanoparticles grown in situ on CdS nanorods for enhanced photocatalytic hydrogen evolution, *ACS Sustain. Chem. Eng.* 7 (2019) 16720–16728.
- [62] B. He, C. Bie, X. Fei, B. Cheng, J. Yu, W. Ho, A.A. Al-Ghamdi, S. Wagh, Enhancement in the photocatalytic H₂ production activity of CdS NRs by Ag₂S and Ni₃ dual cocatalysts, *Appl. Catal. B-Environ.* 288 (2021), 119994.
- [63] Y. Zhang, W. Zhou, J. Wang, L. Jia, L. Liu, X. Tan, T. Yu, J. Ye, Hydrated electrons mediated *in-situ* construction of cubic phase CdS/Cd thin layer on a millimeter-scale support for photocatalytic hydrogen evolution, *J. Colloid Interface Sci.* 607 (2021) 769–781.
- [64] J. Shi, I.U. Islam, W. Chen, F. Wang, Z. Xu, S. Xu, Y. Li, J. Lu, Two-dimensional ultrathin Zn_xCd_{1-x}S nanosheet with exposed polar facet by using layered double hydroxide template for photocatalytic hydrogen generation, *Int. J. Hydrog. Energy* 43 (2018) 19481–19491.
- [65] Y. Wang, Y. Ma, X.-B. Li, L. Gao, X.-Y. Gao, X.-Z. Wei, L.-P. Zhang, C.-H. Tung, L. Qiao, L.-Z. Wu, Unveiling catalytic sites in a typical hydrogen photogeneration system consisting of semiconductor quantum dots and 3d-metal ions, *J. Am. Chem. Soc.* 142 (2020) 4680–4689.
- [66] Z. Luo, H. Zhang, Y. Yang, X. Wang, Y. Li, Z. Jin, Z. Jiang, C. Liu, W. Xing, J. Ge, Reactant friendly hydrogen evolution interface based on di-anionic MoS₂ surface, *Nat. Commun.* 11 (2020) 1116.
- [67] S. Huang, Y. Meng, Y. Cao, F. Yao, Z. He, X. Wang, H. Pan, M. Wu, Amorphous NiWO₄ nanoparticles boosting the alkaline hydrogen evolution performance of Ni₃S₂ electrocatalysts, *Appl. Catal. B-Environ.* 274 (2020), 119120.
- [68] J. Liu, J. Wang, B. Zhang, Y. Ruan, H. Wan, X. Ji, K. Xu, D. Zha, L. Miao, J. Jiang, Mutually beneficial Co₃O₄@MoS₂ heterostructures as a highly efficient bifunctional catalyst for electrochemical overall water splitting, *J. Mater. Chem. A* 6 (2018) 2067–2072.
- [69] I.S. Kwon, T.T. Debelia, I.H. Kwak, Y.C. Park, J. Seo, J.Y. Shim, S.J. Yoo, J.G. Kim, J. Park, H.S. Kang, Ruthenium nanoparticles on cobalt-doped 1T' phase MoS₂ nanosheets for overall water splitting, *Small* 16 (2020), 2000081.